Connectivity between Static Field and Continuous Wave Field Effects on Excitation-Induced H_2 Activation

Yuchen Wang, Christine M. Aikens*

Department of Chemistry, Kansas State University, Manhattan, KS 66506, USA

*Email: cmaikens@ksu.edu

Abstract

Due to the tremendous applications of the plasmon resonance excitation process, such as improvements in catalytic efficiency due to plasmonic enhancement and/or hot electron processes, understanding the mechanism behind these processes has become a popular topic in recent years. In this work, we focus on unraveling the mechanism of excitation-induced H_2 activation using a simplified triangular Au_6/Ag_6 cluster to investigate the effects of the electric field on electron redistribution and bond activation. We applied both static and continuous wave (CW) fields to investigate how these fields affect the systems. Geometrical changes (such as bond lengthening), molecular orbital reordering (affecting the relative energies of orbitals corresponding to hot-electron and charge-transfer excited states), and electronic charge redistribution between the cluster and the adsorbate occur upon application of a static electric field. To study H_2 activation, we apply Ehrenfest dynamics with real-time time-dependent density functional theory (RT-TDDFT) and examine how different excitation frequencies and polarizations affect bond activation. Moreover, electron-only dynamics are examined with RT-TDDFT, and the time-dependent variations in the orbital populations and electronic transitions provide information about the excitation and relaxation processes of hot electrons with applied electric fields. The static field results represent structures that can be accessed during the evolution of the systems when applying continuous wave fields. Through these studies, the effects of static and CW field effects on plasmon-induced H_2 activation can be understood.

Introduction

If an electric field is applied to gold or silver nanoparticles with a frequency corresponding to a plasmonic resonance frequency of the system, the valence electrons of the nanoparticles will be excited and will slosh back and forth collectively.[1–3] This phenomenon is called localized surface plasmon resonance (LSPR), and LSPRs of gold and silver nanoparticles can be utilized in many areas such as photocatalysis, energy conversion, and biological sensing.[4–8] In the field of photocatalysis, plasmonic systems can be designed as catalysts to enhance chemical reactions such as water splitting, CO_2 reduction, H_2 dissociation, and N_2 dissociation.[9–14] A diverse set of plasmonic systems have been designed to accelerate the rate of the plasmon-driven reactions, and active sites on the plasmonic systems have been examined to improve the efficiency of the catalytic reaction.[15–18] According to current understanding, the LSPR process includes many sub-steps such as hot carrier generation, hot carrier relaxation, and thermalization, which cross over a wide range of time scales.[19–24] Due to the complexity of the plasmon-enhanced photocatalytic process, the mechanism behind this process is not yet fully understood. However, it is of interest to understand this mechanism so that the efficiency of the process can be improved. In this work, we focus on studying plasmon-induced H_2 activation because H_2 activation is one of the most important steps in many chemical engineering processes such as syngas conversion and energy storage.[25,26] In addition, H_2 is the simplest diatomic molecule, and choosing this simple model may help us find the fundamental principles in the plasmon-driven process and guide us in further studies of more complex systems.

The plasmonic properties of both gold and silver nanoclusters have been studied experimentally and theoretically in previous literature, and silver and gold exhibit both similarities and differences in the electronic transitions involved in the plasmon resonance process.[27–31] Generally, the intense dipolar plasmonic resonance peak can be observed with a smaller size of silver nanoclusters compared to gold clusters.[32,33] Silver and gold nanoclusters also show differences in excited states energy distribution and types of electronic transition processes upon excitation.

The experimental work typically employs large nanoparticles that exhibit strong plasmon resonances; however, these large nanoparticles would require high computational memory and runtime costs to model theoretically. Therefore, finding an applicable model to investigate the plasmon-excitation process is necessary. To study the photo-dissociation of small molecules in the

presence of an Au nanoparticle, the jellium model has previously been applied which treats the nanoparticle as a uniform charge density to reduce the computational cost.[12] Other theoretical methods that explicitly consider the nuclei have also been considered.[34–43] Time-dependent density functional theory (TDDFT) has been employed to study plasmon-enhanced photocatalysis with small nanoparticles.[39–42] Computational methods with less expensive costs (i.e., TD-DFTB[34–36] and TDDFT+TB[37,38]) have been developed to deal with larger-sized nanoparticles. In addition, mixed levels of computational methods have been used to study the plasmon-induced H_2 dissociation on an Au(111) slab, in order to reach a balance between computational accuracy and cost.[9]

Au_6/Ag_6 has been demonstrated as a reasonable model and its structure and properties have been calculated and discussed in previous research.[41,44,45] In recent years, the photo-dissociation of H_2 and the corresponding potential energy surfaces for interaction with a triangular Au_6 system have been studied using DFT and TDDFT methods.[41] Excited potential energy surfaces corresponding to hot electrons (electronically excited surfaces corresponding to the metal cluster) and charge transfer surfaces (involving adsorbate antibonding orbitals) were considered.[41] Therefore, although a triangular metal cluster does not have a plasmon, it can still be considered a promising simplified model to study how excitation affects catalytic properties.

In this work, we applied the Au_6/Ag_6 cluster as a model to investigate how electric fields affect the excitation-induced activation of the H_2 molecule. One question that will be answered is: what insights can be achieved by applying a static electric field (which mimics extrema of a continuous wave (CW) field)? We find that static electric field calculations provide insights into geometrical structure changes (such as bond lengthening processes), molecular orbital reordering (which affects the relative energies of orbitals corresponding to hot-electron and charge-transfer excited state surfaces), and the division of the electronic charge distribution between the cluster and the adsorbate. To study the static electric field effects, fields with different strengths are applied during the optimization of the structures. Next, we apply a CW field in order to examine electron and electron-nuclear dynamics in this system. Excited state dynamics is considered an essential tool when studying the dynamic processes of electron-electron scattering and electron-phonon coupling in the plasmonic resonance process.[20,46,47] To study H_2 activation, we apply Ehrenfest dynamics, which is a mean-field nonadiabatic dynamics that is employed to study the motion of both nuclei and electrons in excited states.[48–50] For the excitation-induced activation

process arising from the silver/gold cluster, the system will yield different responses under different excitation frequencies and polarizations. Therefore, this work also focuses on the question: how do excitation frequencies and polarization affect the activation process? Therefore, the CW field was then applied to investigate the systems using frequencies corresponding to certain excitation modes. Electronic dynamics are investigated using real-time TDDFT methods[51,52] and coupled electron-nuclear dynamics are analyzed using Ehrenfest dynamics.[48,49] Real-time TDDFT provides information about electronic transitions and population, which gives us an understanding of the hot-carrier generation and hot-electron relaxation processes with different applied electric fields.

Computational methods

We first applied both PBE[53] and LC-ωPBE[54] functionals to calculate the geometric structures of Au_6H_2 and Ag_6H_2. PBE and LC-ωPBE show consistent trends when calculating the Ag_6H_2 system; however, H_2 is calculated to bind with an angle to the Au cluster using applied electric fields in the PBE calculations (Table S1). Moreover, the Au_6 nanocluster itself also becomes bent in the geometry optimization process with applied electric fields using the PBE functional. Because the long-range corrected (LC) functionals are expected to be more accurate for metal-adsorbate interactions, all of the following calculations were performed at the LC-ωPBE[54]/LanL2DZ[55–57] level of theory using a development version of the Gaussian software package.[58] The lowest energy structures when H_2 on the nanocluster vertex are shown in Figure 1.

When studying the effects of a static electric field, the geometry was optimized with an applied static field. The electric field is applied along the z axis (Figure 1), and the strengths of the fields were chosen to be 0.01 au (3.57×10^{14} W/cm^2), 0.005 au (1.79×10^{14} W/cm^2), and 0.001 au (3.57×10^{13} W/cm^2), respectively. The electric fields were chosen based on previous work that shows very weak activation of H_2 (coupled with an Ag_8 nanowire) with a CW electric field strength of 0.001 au and slightly stronger activation for 0.01 au.[39] Electric fields were applied in both the positive z (Z+) and negative z (Z-) directions, which correspond to the maxima of the CW fields.

Linear-response (LR) TDDFT calculations were performed with zero applied field to obtain the absorption spectra, which provides information about frequencies of interest (analogous to LSPR frequencies) that will be used in electron-only RT-TDDFT (henceforth referred to simply

as RT-TDDFT) and combined electron-nuclear (Ehrenfest) calculations. For both RT-TDDFT and Ehrenfest dynamics calculations, a CW electric field is applied for the first 20 fs of total simulation; the field is ramped up during the first 1 fs and then ramped down during the final 1 fs, giving a trapezoidal envelope overall. The maximum strength of the applied electric field is 0.01 au (3.57×10^{14} W/cm^2). Though this is a higher field strength than most experimental CW fields, this compensates in part for the short duration of the field application. Moreover, previous work has shown that smaller nanoclusters typically require stronger applied fields for adsorbate activation, but this decreases with cluster size. [36,59] For RT-TDDFT calculations, the electronic step is set to 0.002 fs. For the Ehrenfest dynamics, the electronic step size is 0.00025 fs and the nuclear step size is 0.1 fs, and the initial velocity of all the systems is set as zero. All of the RT-TDDFT and Ehrenfest calculations were performed using a development version of the Gaussian software package[58] written by Xiaosong Li and co-workers.[48,60,61]

Results and discussion

Static fields effect

1. Geometric information

For the ground state geometry optimizations, the Au_6/Ag_6 cluster was oriented in the yz plane and the H_2 molecules were initially placed parallel to the x, y, and z axes. The lowest energy isomer has H_2 parallel to the x axis for both the Ag_6H_2 and Au_6H_2 systems (Figure 1). The H-H bond length is 0.75 Å in the ground state for both systems. The distance between the H_2 and the gold cluster (2.41 Å) is smaller than with the silver cluster (3.22 Å) for the zero-field equilibrium structure (Table 1). In addition, the binding energy between the H_2 and the gold cluster (6.41 kJ/mol) is higher than with the silver cluster (2.90 kJ/mol) for the zero-field equilibrium structure (using the equation E(binding) = E(H_2) + E(bare cluster) - E(H_2-cluster system)), indicating a stronger bond between the H_2 adsorbate and the gold cluster.

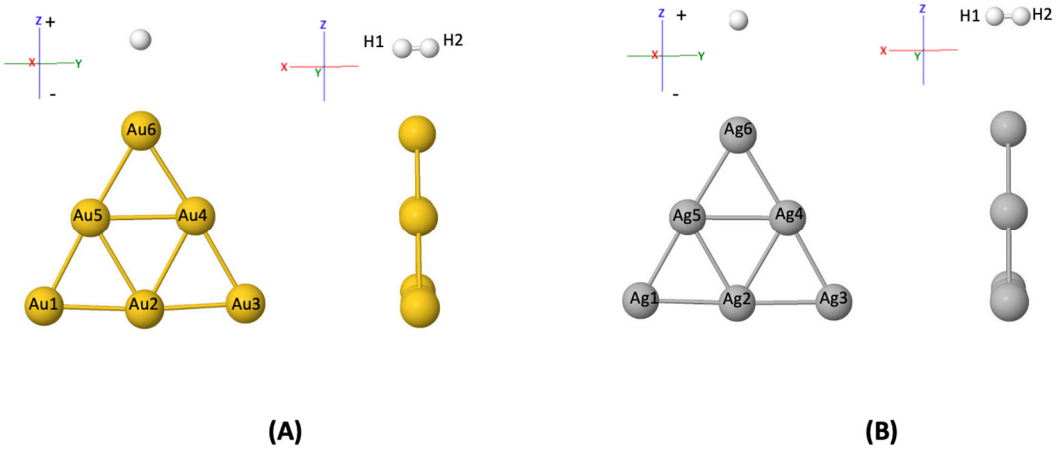

Figure 1. Optimized geometries of A. Au_6H_2 and B. Ag_6H_2 systems at zero applied electric field

Table 1. Selected bond length information (Å) for Au_6H_2 and Ag_6H_2 systems optimized with static applied electric fields. Atom numbers are provided in Figure 1.

		- 0.01 au	- 0.005 au	- 0.001 au	Zero field	0.001 au	0.005 au	0.01 au
	H1-H2	0.77	0.77	0.76	0.75	0.75	0.75	0.75
Au_6H_2	Au6-H1	2.10	2.18	2.33	2.41	2.53	3.25	3.27
	Au6-H2	2.10	2.18	2.33	2.41	2.53	3.33	4.02
	H1-H2	0.76	0.75	0.75	0.75	0.75	0.75	0.74
Ag_6H_2	Ag6-H1	2.34	3.19	3.22	3.22	3.46	4.15	4.93
	Ag6-H2	2.34	3.19	3.22	3.22	3.46	4.15	4.93

For the Au_6H_2 system, when a static electric field is applied in the positive direction along the z-axis (Z+ direction), the H_2 bond length stays the same, but H_2 is rotated from the x-preferred configuration (with H_2 parallel to the x-axis) to the z-preferred configuration (H_2 parallel to the z-axis) as the applied field increases. However, H_2 stays in the x-preferred configuration with Z+ electric fields for the Ag_6H_2 system and the H-H bond length decreases with the more intense field. In the Z- direction, H_2 stays in the x-preferred configuration and the H_2 bond length increases with more intense electric fields for both Ag_6H_2 and Au_6H_2 systems. With the increasing field strength in the Z- direction, we can observe the Au6-H and Ag6-H distances decrease; however, with the increasing field strength in the Z+ direction, we can observe the Au6-H and Ag6-H distances

increase. Therefore, the applied fields in the negative direction shorten the distance between the cluster and the H_2 molecule while simultaneously increasing the H-H bond length, suggesting that these fields lead towards chemisorption of hydrogen, and the applied fields in the positive direction will potentially lead H_2 to desorb from the cluster.

2. Effects of static electric fields on the molecular orbital diagram

In addition to the geometric changes described above, the applied electric field also leads to modification of molecular orbital energies and the orbital characters in the systems. Molecular orbitals for the optimized structures with zero applied field and for the 0.01 au Z+ and Z- fields are shown in Figure 2 for Ag_6H_2 and Figure S1 for Au_6H_2. For Ag_6H_2, the HOMO shows antibonding character between H_2 and the cluster for zero applied field and for the Z+ 0.01 au field. However, this type of orbital character switches to the HOMO-1 for the Z- 0.01 au field. The orbital with H_2 σ^* antibonding character is LUMO+5 for the Z- 0.01 au field, LUMO+6 for the zero applied field, and LUMO+7 for the Z+ 0.01 au field. The switching of the order of the molecular orbital character with different field strengths can also be observed in the Au_6H_2 system (Figure S1), which is consistent with previous literature that examined the ordering of this orbital as a function of H-H and Au-H distances, although the previous work did not examine static applied fields.[41] The crossing of orbitals with different character in the correlated molecular orbital diagrams indicates that the applied static field will modify the ordering of orbitals with different character, which is expected to lead to variations in orbital populations and electronic transitions as a function of different applied fields. For both Au_6H_2 and Ag_6H_2 systems, the applied field has the largest effects on the orbital energies of LUMO, LUMO+2, and LUMO+5 (Figure S2). Because occupation of antibonding orbitals is considered to be a possible mechanism to induce photocatalysis, this implies that application of an electric field (whether static or time-varying) may affect the orbital energies and thus the ability to access states involving these orbitals.

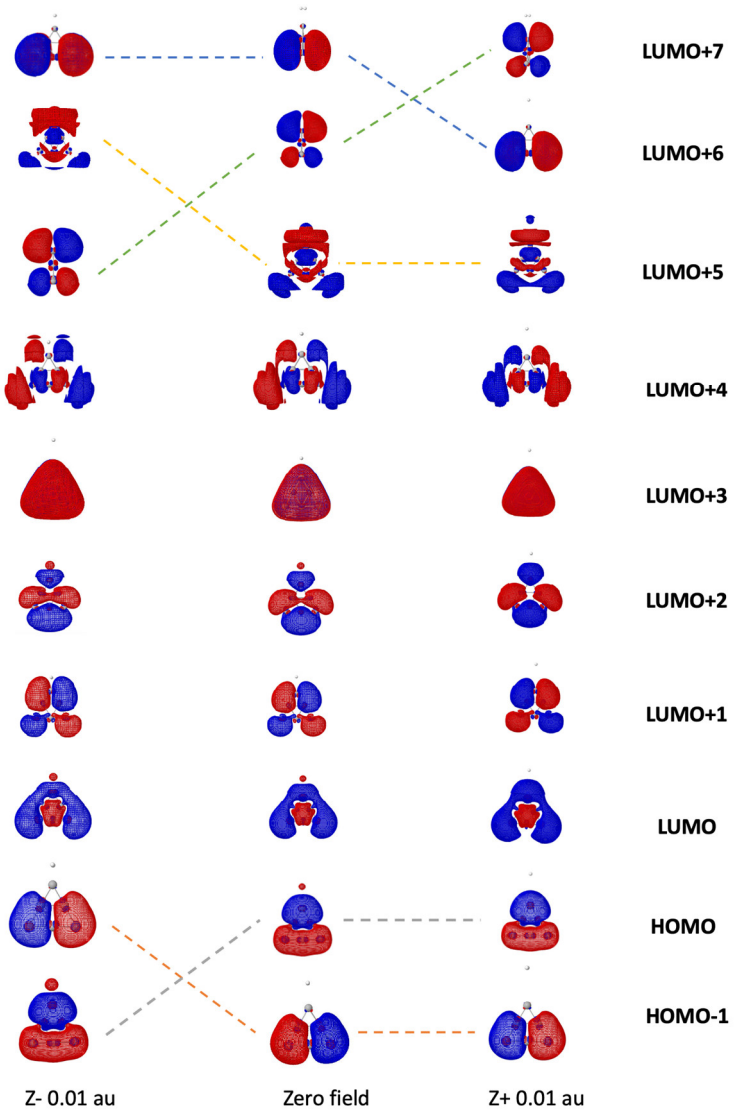

Figure 2. Selected molecular orbitals of optimized Ag_6H_2 under different static applied electric fields. (All molecular orbitals are oriented using a front view, except the orbitals involving H_2 σ*, which are oriented using the side view for the sake of clarity.)

3. Interactions between H_2 and Au_6/Ag_6 cluster

To study the interaction between H_2 and the clusters, we examine the orbitals responsible for bonding between the two subsystems. The molecular orbital that contains bonding character between the H_2 σ orbital and the Au_6 or Ag_6 cluster lies relatively low in energy (orbital index of 25; Figure 3) and the corresponding molecular orbital with antibonding character lies close to the

fermi energy (HOMO or HOMO-1, depending on the applied field). The selected orbital energies are shown in Table S2. For the Z- 0.01 au field, orbital 57 (HOMO-1) shows antibonding character between the H_2 molecule and the Ag_6/Au_6 cluster. With the decrease of the field strength in the Z- direction (to Z- 0.001 au), the antibonding character shifts to orbital 58 (HOMO). For the Z+ field, there is less interaction between the molecule and cluster as the field strength increases (Figure 3).

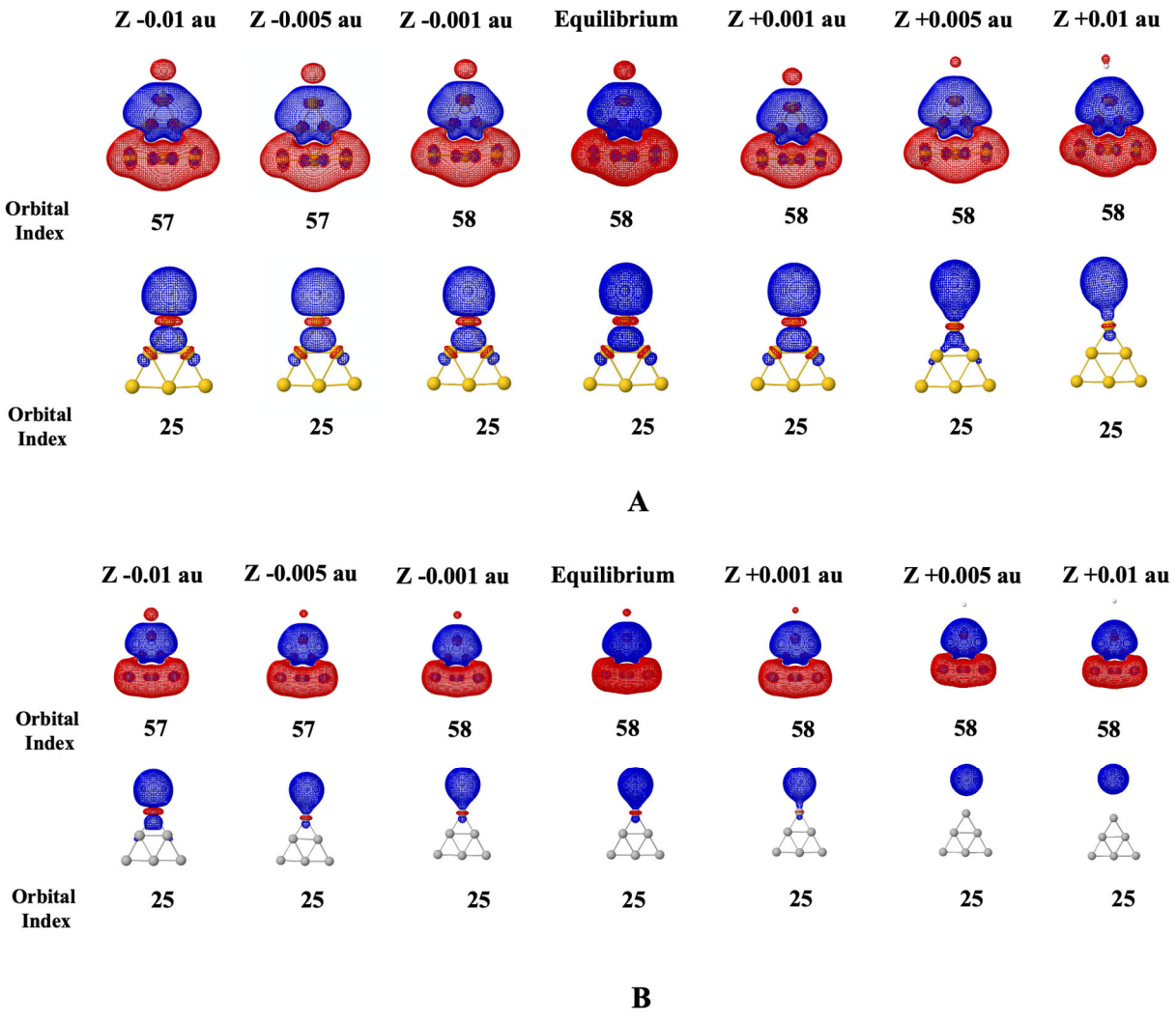

Figure 3. Bonding and antibonding characters between cluster and H_2 molecule. A. Au_6H_2 and B. Ag_6H_2

Selected orbital energy differences are shown in Figure 4. “Bonding” denotes the orbital that shows bonding character for the interaction between H_2 and the cluster (orbital index 25); “antibonding” denotes the orbital that shows antibonding character for the interaction between H_2 and the cluster (orbital index 57 or 58). Generally, orbital energy differences between bonding and antibonding orbitals show similar trends as the orbital energy differences between the LUMO and the bonding orbital with the applied field. The increased energy difference with a more intense field strength in the Z- direction indicates a stronger coupling between H_2 and the clusters. For the Ag_6H_2 system, the orbital energy differences show a significant decrease when the applied field was decreased from 0.01 au to 0.005 au in the Z- direction. However, the orbital energy differences stay relatively stable in other applied fields. For the Au_6H_2 system, a significant orbital energy difference change occurs when the electric field shifts from Z+ 0.001 au to the Z+ 0.005 au field, and the change may result from the rotation of the H_2 molecule in the system with a stronger static field.

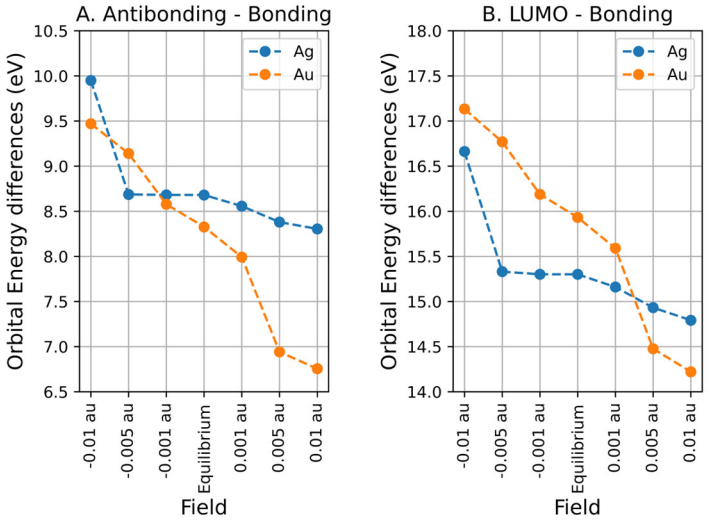

Figure 4. Orbital energy differences between A. bonding and antibonding orbitals, B. LUMO and bonding character orbitals with the change of applied field.

4. Partial charge analysis

To investigate the static field effect on the charge distribution of the systems, the Mulliken (Figure 5) and Hirshfeld (Figure S3) partial charge approaches were applied to analyze the partial charges on the atoms. For both the Ag_6H_2 and Au_6H_2 systems, the partial charge on the H atom is

the most positive for the Z- 0.01 au field and shows a monotonic decrease as the Z- field strength decreases and as the field switches to the Z+ direction, indicating that the more intense field along the Z- direction leads to a greater degree of charge transfer between H_2 and the cluster. For both Mulliken and Hirshfeld charge analysis approaches, the sum of the charges on the H atoms when interacting with the Au cluster is larger than for the interaction with the Ag cluster, indicating that there is more charge transfer in Au_6H_2 than in the Ag_6H_2 system.

For the Ag_6H_2 system, the partial charge on the Ag6 atom shows a monotonic decrease with the applied field (except for the Z+ 0.01 au field) using both Mulliken charge and Hirshfeld charge analysis. For the Au_6H_2 system, the Mulliken charge on the Au6 atom shows a monotonic increase with the applied field (except for the Z+ 0.01 au field), and the Hirshfeld charge on Au6 shows a monotonic decrease with the applied field. The above analysis indicates that the applied static field will affect the partial charge distribution of the system, and the partial charge on the hydrogen atoms shows a general correlation with field strength. Similar to Au6, both Au1 and Au3 (which are also vertex atoms) become more negatively charged as the static field becomes greater in the Z- direction.

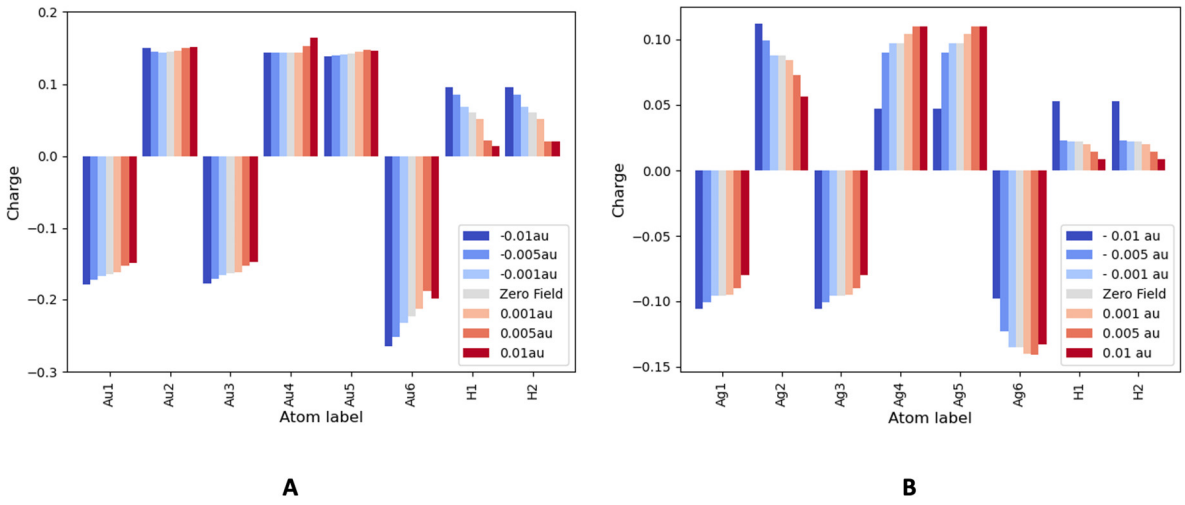

Figure 5. Mulliken charge analysis for A. Au_6H_2 B. Ag_6H_2.

Resonant electric fields

1. Linear response TDDFT

The zero-field absorption spectra of Au_6H_2 and Ag_6H_2 were calculated using linear response TDDFT (Figure 6). Ag_6H_2 displays peaks with a greater absorption strength than Au_6H_2 in the range of 3-5 eV, and the strongest peaks in the Ag_6H_2 spectrum are consistent with previous reports.[32,33] For the Au_6H_2 system, excitation 1 and excitation 3 show the two most intense peaks out of the first five peaks from the absorption spectrum. Both peak 1 (excitation 1) and peak 3 (excitation 3) show dominant polarization along the y and z axes, corresponding to the plane of the metal cluster. Compared with Au_6H_2, the Ag_6H_2 system shows two intense dipolar peaks at 3.16 eV (excitation 1) and 3.64 eV (excitation 2); both excitation 1 and excitation 2 (which includes two excited states) are polarized along the y and z axes. For the absorption spectrum of Ag_6H_2, excitation 3 is located at 4.97 eV and is polarized along the x-axis. The strong peaks from the LR-TDDFT calculations are used to select frequencies for applied electric fields that will selectively excite particular excitations within the cluster systems. In the next step, external electric fields with those selected frequencies will be applied to the system and Ehrenfest dynamics will be used to simulate the excitation-induced H_2 activation process when interacting with Au/Ag clusters.

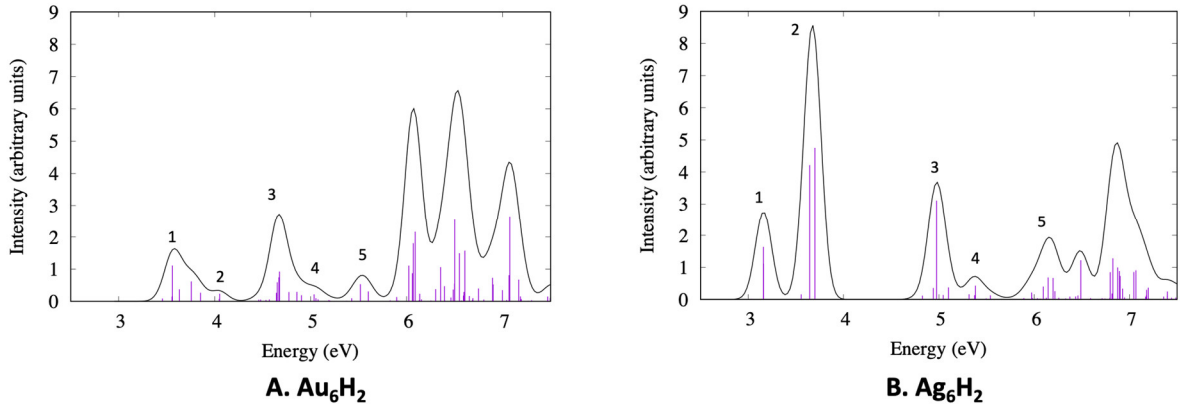

Figure 6. Linear absorption spectra for A. Au_6H_2 B. Ag_6H_2.

2. Nonadiabatic dynamics results

To examine the H_2 bond distance change in the excitation-induced catalytic process, Ehrenfest dynamics were carried out. For the Au_6H_2 system, the applied electric fields were

selected to be resonant with excitations 1 and 3 from Figure 6A, with all three polarization directions examined for each excitation (Figure 7). For the Ag_6H_2 system, fields were chosen to be resonant with excitations 1, 2, and 3 from Figure 6B, also with all three polarization directions (Figure 8). All simulations were performed with the 0.01 au external field strength. Dynamics were performed over a time period of 100 fs.

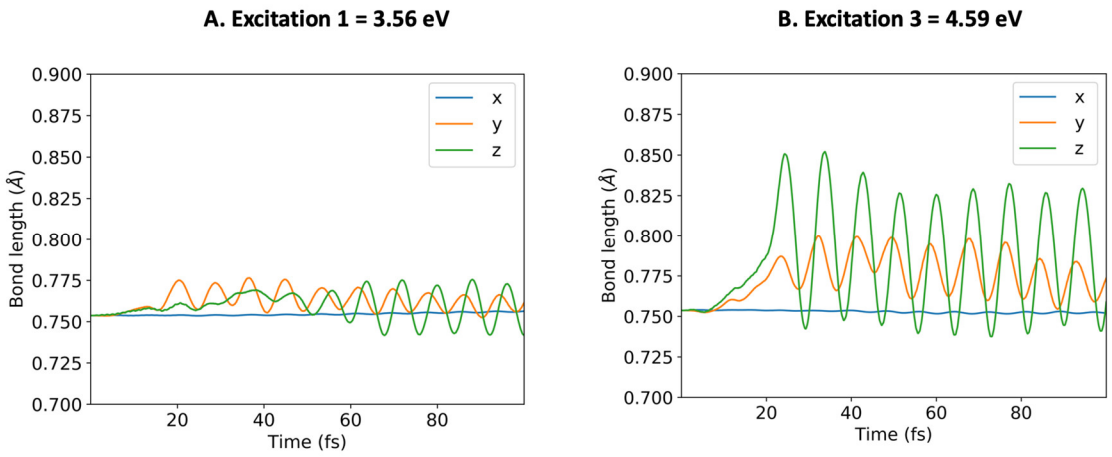

Figure 7. Variation of H-H bond distance during Ehrenfest dynamics simulations for the Au_6H_2 system with the 0.01 au electric field strength.

For the Au_6H_2 Ehrenfest dynamics results (Figure 7), if the electric field has a frequency corresponding to 3.56 eV (excitation 1), the bond length results show H-H stretching within 100 fs. The maximum H-H bond distance was found to be 0.775 Å for both y- and z-polarized fields, and the H-H bond distance is essentially unchanged for the x-polarized field. For an applied electric field corresponding to 4.59 eV (excitation 3), the H-H bond shows more intense bond stretching for simulations with the y- and z-polarized fields compared with those resonant with excitation 1, and the maximum H-H bond distance reaches up to 0.850 Å for the simulation with z-polarization and 0.800 Å with y-polarization. From the linear response TDDFT spectrum, peak 3 shows a higher absorption strength than peak 1, which correlates with the greater activation of the H-H bond.

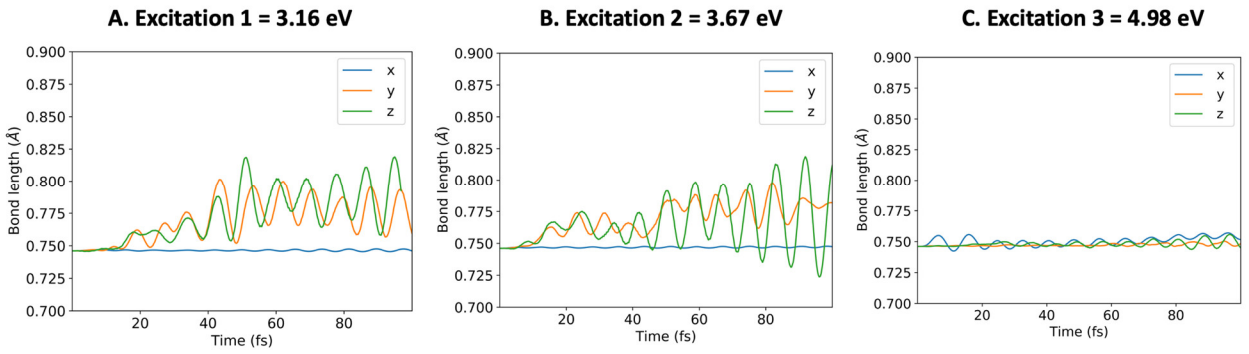

Figure 8. Variation of H-H bond distance during Ehrenfest dynamics simulations for the Ag_6H_2 system with the 0.01 au electric field strength.

For the Ag_6H_2 system, for the simulations resonant with excitation 1 (3.16 eV) with y- and z-polarized electric fields, the H-H distance is stable for the first 10 fs, and then displays bond stretching from 20 ~ 100 fs, for which the maximum bond distance can reach up to 0.800 Å (at around 45 fs) with the y-polarized field and 0.820 Å (at around 50 fs) with the z-polarized electric field. For simulations resonant with excitation 2, with the y-polarized electric field the maximum bond distance can reach 0.800 Å (at around 85 fs), and with the z-polarized electric field the maximum bond distance can reach 0.825 Å (at around 95 fs). Although excitation 2 (3.67 eV) has a stronger oscillator strength than excitation 1, the overall bond activation is similar for both simulations. For the simulation resonant with excitation 3 (4.98 eV), the excitation shows a transition dipole moment along the x direction based on LR-TDDFT calculations. However, only weak bond stretching is observed with x-, y-, and z- polarized fields, and the H-H distances do not become longer than 0.775 Å within 100 fs.

The above results indicate that the polarization of the electric field affects the H_2 activation. Ideally, the electric field should have the same polarization as the transition dipole moment of that excitation in order to excite the system, and we observe that the H_2 is not activated if the electric field is polarized along the x axis with excitation 1 and 2 simulations for Ag_6H_2 (Figure 8a and Figure 8b); as mentioned above, excitations 1 and 2 have transition dipole moments along the y and z axes. However, electric field polarization is not the only factor that determine the H_2 activation, because the simulation shown in Figure 8c indicates that H_2 cannot be activated even when the electric field has the same frequency and is polarized along the same direction as the transition dipole moment of excitation 3. Overall, excitations polarized in the plane of the metal cluster lead to greater adsorbate bond activation.

3. Real-time TDDFT calculations

RT-TDDFT can be performed with fixed nuclei in order to determine electron-only dynamics. RT-TDDFT simulations were performed to determine the orbital populations (Figure 9 and Figure 10) and electronic transitions (Figure S4 and Figure S5) using the applied electric fields of interest.

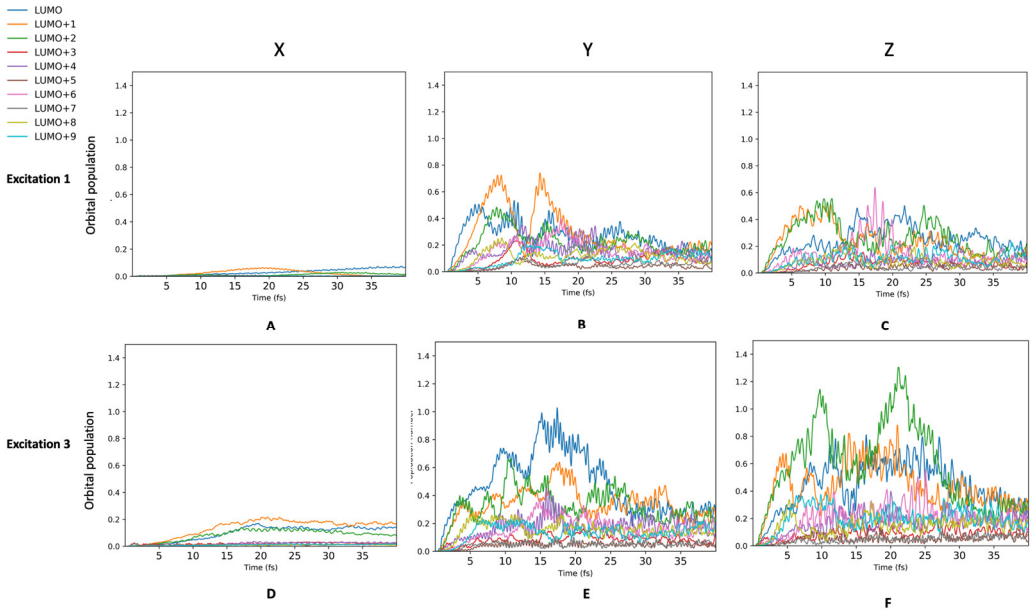

Figure 9. Orbital population analysis of Au_6H_2 system in RT-TDDFT simulations

Orbital population results for the Au_6H_2 system (Figure 9) indicates that there is almost no orbital population transfer to unoccupied orbitals if the electric field is polarized along the x-axis. We can also observe from Figure 9 that more electrons were transferred to the unoccupied orbitals with the field resonant with excitation 3 compared to excitation 1. This can be correlated to the Ehrenfest dynamics results that H-H bonds shows more intense stretching when the frequency corresponds to excitation 3 rather than excitation 1.

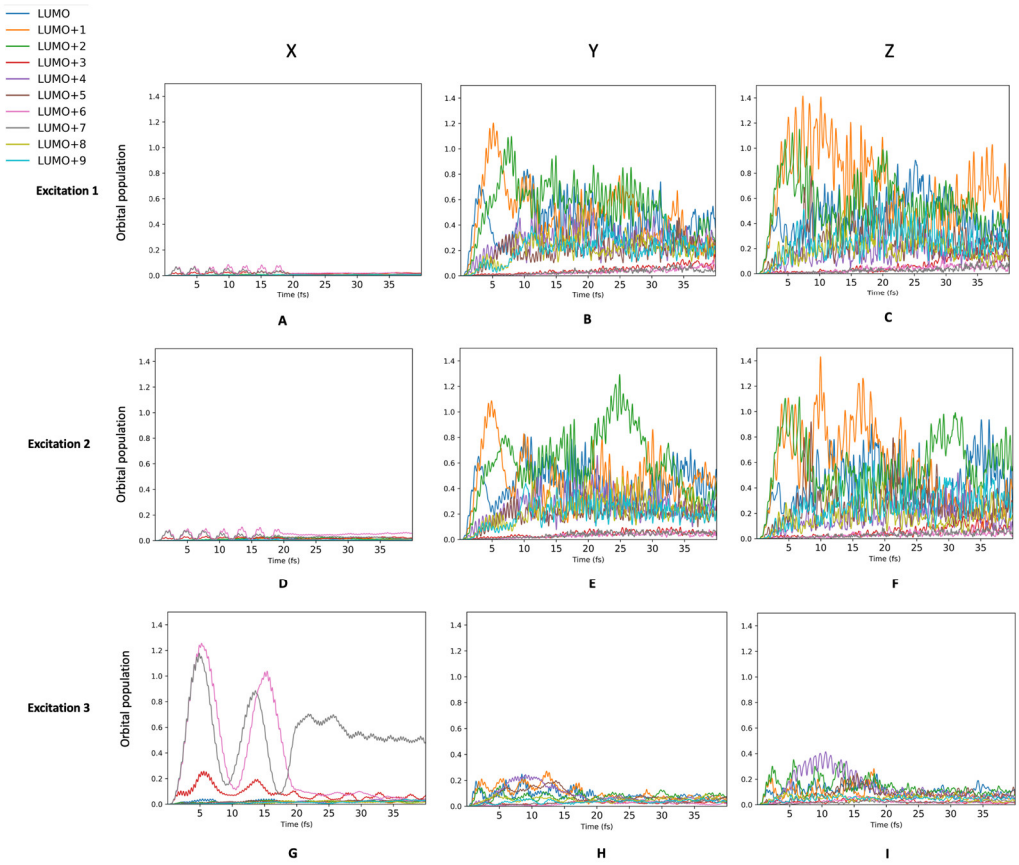

Figure 10. Orbital population analysis of Ag_6H_2 system in RT-TDDFT simulations.

For the Ag_6H_2 system, electron-only dynamics results indicate that electron population negligibly transfers into the unoccupied orbitals using the x-polarized electric field when the field is resonant with either excitation 1 or excitation 2. These electron-only dynamics results can be correlated with the Ehrenfest dynamics results in which the H_2 distance stays almost constant during the 100 fs of simulation using x-polarized fields resonant with these two excitations. When the electric field is applied along the y direction for excitation 1, the orbital population of LUMO+1 reaches its highest peak from ~5-6 fs and the population of LUMO+2 reaches its highest peak from ~7-10 fs. LUMO+1 and LUMO+2 play the dominant role for the first 40 fs. For excitation 2, the maximum population of LUMO+1 is lower than for excitation 1 and the population of LUMO+2 reaches its highest peak at around 25 fs, which is 5 fs after the electric field is turned off.

When the electric field is applied along the z direction for excitation 1, the population of LUMO+1 ramped up to 1.4 during ~0-10 fs, and the orbital population of LUMO+2 ramped up to 1.1 during ~0-5 fs. For excitation 3, the populations of LUMO+1 and LUMO+2 share similar

trends during ~0-7 fs; however, the population of LUMO+2 ramped down at 10 fs while LUMO+1 population ramped up to reach a maximum peak (with a population number around 1.4).

For excitation 3, electron-only dynamics results show low orbital population transfer with the y and z polarized electric fields. However, with the x polarization, significant population can be observed in LUMO+6 and LUMO+7 during the first 20 fs. Both LUMO+6 and LUMO+7 show two intense peaks at about 5 fs and 15 fs. After 20 fs, the population of LUMO+7 decreases to 0.6 and stays stable across 25-40 fs, and the population of LUMO+6 decreases to 0.1 over 25-40 fs. Since the Ehrenfest dynamics results show that H_2 cannot be activated if the electric field has a frequency corresponding to excitation mode 3 (for all three polarization directions), this demonstrates that electron population is not the only factor that determines the H_2 activation, and H_2 may not be activated even when initially unoccupied orbitals gain electron population upon electric field excitation. It also suggests that electron population in particular types of orbitals is less important than others; interestingly, LUMO+6 is the H_2 σ^* orbital, which would be a logical target for catalysis, yet appears to be unimportant for H_2 activation in this case.

Conclusions

In this work, we compared the factors involved with activation of adsorbates via excited state activation of silver and gold clusters. First, static electric fields with different varying strengths were applied and we found that both the geometric information and electronic structures were modified with different field strengths and directions. Geometrically, strong positive static fields in the z direction led to a bent adsorbate being preferred for Au_6H_2, while Ag_6H_2 maintained its zero-field orientation. The H-H bond distance increased with increasingly negative static fields, suggesting bond activation is induced by the negative z-direction portion of a CW wave field rather than the positive z-direction portion. Simultaneously, the Au-H bond decreases in length as the field is applied in the negative z direction. Overall, this suggests that the time-varying fields in a CW excitation will alternately increase and decrease the H-H bond length, while also alternately decreasing and increasing the Au-H bond length, leading to excitation. The molecular orbital diagram changes and partial charge analysis results indicate that the applied field also leads to changes in the electronic structure of the system, and we can observe the crossing of the orbital character with different applied electric fields. Moreover, the applied electric field affects the

coupling between the bonding/antibonding of the H_2 σ orbital with the Au/Ag cluster, with the negative z direction field increasing the coupling.

Continuous wave fields with different excitation frequencies were then applied to study how the H_2 adsorbate is activated using the excited state dynamics induced by the silver and gold clusters. The electric fields were polarized along x, y and z for each frequency. Ehrenfest dynamics results indicate that the H_2 activation not only depends on the frequencies of the excitation, but also depends on the configuration between the Ag/Au cluster and the H_2 molecule. Moreover, it shows that H_2 is not activated with an x-polarized field even when the excitation has its transition dipole moment along the x-axis and activates the σ* orbital of the H_2. Instead, the most important excitations correspond to "hot electron" states of the gold or silver cluster. Linear response TDDFT results show that Ag has more intense peaks than Au; however, both of these systems show similar trends in H_2 activation with selected excitations. Therefore, oscillator strength is not the only factor that determines the activation properties, and the nuclear motions play an important role in this excitation-induced process.

Supporting information

Comparison between PBE and LC-ωPBE functionals, correlated MO diagram of the Au_6H_2 system, orbital energies of selected orbitals, Hirshfeld charge analysis and electronic transitions in RT-TDDFT simulations.

Acknowledgments

This material is based on work supported by the Department of Energy under grant DE-SC0012273. The computing for this work was performed on the Beocat Research Cluster at Kansas State University, which is in part funded by the NSF (Grant Nos. CHE-1726332, CNS-1006860, EPS-1006860, and EPS-0919443). The authors thank Prof. Xiaosong Li for the RT-TDDFT and Ehrenfest Dynamics code.

References

(1) Kelly, K. L.; Coronado, E.; Zhao, L. L.; Schatz, G. C. The Optical Properties of Metal Nanoparticles: The Influence of Size, Shape, and Dielectric Environment. *J. Phys. Chem. B* **2003**, *107* (3), 668–677.

(2) Mulvaney, P. Surface Plasmon Spectroscopy of Nanosized Metal Particles. *Langmuir* **1996**, *12* (3), 788–800.

(3) Hartland, G. V. Optical Studies of Dynamics in Noble Metal Nanostructures. *Chem. Rev.* **2011**, *111* (6), 3858–3887.

(4) Mou, T.; Quiroz, J.; Camargo, P. H. C.; Wang, B. Localized Orbital Excitation Drives Bond Formation in Plasmonic Catalysis. *ACS Appl. Mater. Interfaces* **2021**, *13* (50), 60115–60124.

(5) Hooshmand, N.; Thoutam, A.; Anikovskiy, M.; Labouta, H. I.; El-Sayed, M. Localized Surface Plasmon Resonance as a Tool to Study Protein Corona Formation on Nanoparticles. *J. Phys. Chem. C* **2021**, *125* (45), 24765–24776.

(6) Kim, H. Y.; Henkelman, G. CO Oxidation at the Interface between Doped CeO_2 and Supported Au Nanoclusters. *J. Phys. Chem. Lett.* **2012**, *3* (16), 2194–2199.

(7) Aslam, U.; Rao, V. G.; Chavez, S.; Linic, S. Catalytic Conversion of Solar to Chemical Energy on Plasmonic Metal Nanostructures. *Nat. Catal.* **2018**, *1* (9), 656–665.

(8) Hou, W.; Cronin, S. B. A Review of Surface Plasmon Resonance-Enhanced Photocatalysis. *Adv. Funct. Mater.* **2013**, *23* (13), 1612–1619.

(9) Mukherjee, S.; Libisch, F.; Large, N.; Neumann, O.; Brown, L. V.; Cheng, J.; Lassiter, J. B.; Carter, E. A.; Nordlander, P.; Halas, N. J. Hot Electrons Do the Impossible: Plasmon-Induced Dissociation of H_2 on Au. *Nano Lett.* **2013**, *13* (1), 240–247.

(10) Zhou, L.; Zhang, C.; McClain, M. J.; Manjavacas, A.; Krauter, C. M.; Tian, S.; Berg, F.; Everitt, H. O.; Carter, E. A.; Nordlander, P.; Halas, N. J. Aluminum Nanocrystals as a Plasmonic Photocatalyst for Hydrogen Dissociation. *Nano Lett.* **2016**, *16* (2), 1478–1484.

(11) Douglas-Gallardo, O. A.; Box, C. L.; Maurer, R. J. Plasmonic Enhancement of Molecular Hydrogen Dissociation on Metallic Magnesium Nanoclusters. *Nanoscale* **2021**, *13* (25), 11058–11068.

(12) Zhang, Y.; Nelson, T.; Tretiak, S.; Guo, H.; Schatz, G. C. Plasmonic Hot-Carrier-Mediated Tunable Photochemical Reactions. *ACS Nano* **2018**, *12* (8), 8415–8422.

(13) Kumari, G.; Zhang, X.; Devasia, D.; Heo, J.; Jain, P. K. Watching Visible Light-Driven CO $_2$ Reduction on a Plasmonic Nanoparticle Catalyst. *ACS Nano* **2018**, *12* (8), 8330–8340.

(14) Monyoncho, E. A.; Dasog, M. Photocatalytic Plasmon-Enhanced Nitrogen Reduction to Ammonia. *Adv. Energy Sustain. Res.* **2021**, *2* (3), 2000055.

(15) Jiang, W.; Low, B. Q. L.; Long, R.; Low, J.; Loh, H.; Tang, K. Y.; Chai, C. H. T.; Zhu, H.; Zhu, H.; Li, Z.; Loh, X. J.; Xiong, Y.; Ye, E. Active Site Engineering on Plasmonic Nanostructures for Efficient Photocatalysis. *ACS Nano* **2023**, acsnano.2c12314.

(16) Sayed, M.; Yu, J.; Liu, G.; Jaroniec, M. Non-Noble Plasmonic Metal-Based Photocatalysts. *Chem. Rev.* **2022**, *122* (11), 10484–10537.

(17) Yanagi, R.; Zhao, T.; Solanki, D.; Pan, Z.; Hu, S. Charge Separation in Photocatalysts: Mechanisms, Physical Parameters, and Design Principles. *ACS Energy Lett.* **2022**, *7* (1), 432–452.

(18) Zhan, C.; Yi, J.; Hu, S.; Zhang, X.-G.; Wu, D.-Y.; Tian, Z.-Q. Plasmon-Mediated Chemical Reactions. *Nat. Rev. Methods Primer* **2023**, *3* (1), 12.

(19) Hartland, G. V.; Besteiro, L. V.; Johns, P.; Govorov, A. O. What's so Hot about Electrons in Metal Nanoparticles? *ACS Energy Lett.* **2017**, *2* (7), 1641–1653.
(20) Zhang, Y. Theory of Plasmonic Hot-Carrier Generation and Relaxation. *J. Phys. Chem. A* **2021**, *125* (41), 9201–9208.
(21) Román Castellanos, L.; Hess, O.; Lischner, J. Single Plasmon Hot Carrier Generation in Metallic Nanoparticles. *Commun. Phys.* **2019**, *2* (1), 47.
(22) Christopher, P.; Moskovits, M. Hot Charge Carrier Transmission from Plasmonic Nanostructures. *Annu. Rev. Phys. Chem.* **2017**, *68* (1), 379–398.
(23) Khurgin, J. B. Hot Carriers Generated by Plasmons: Where Are They Generated and Where Do They Go from There? *Faraday Discuss.* **2019**, *214*, 35–58.
(24) Cortés, E.; Besteiro, L. V.; Alabastri, A.; Baldi, A.; Tagliabue, G.; Demetriadou, A.; Narang, P. Challenges in Plasmonic Catalysis. *ACS Nano* **2020**, *14* (12), 16202–16219.
(25) Satyapal, S.; Petrovic, J.; Read, C.; Thomas, G.; Ordaz, G. The U.S. Department of Energy's National Hydrogen Storage Project: Progress towards Meeting Hydrogen-Powered Vehicle Requirements. *Catal. Today* **2007**, *120* (3–4), 246–256.
(26) Luo, J.; Liu, J.-X.; Li, W.-X. H_2 Activation on Pristine and Substitutional ZnO($10\bar{1}0$) and Cr_2O_3 (001) Surfaces by Density Functional Theory Calculations. *J. Phys. Chem. C* **2022**, *126* (21), 9059–9068.
(27) Berdakin, M.; Douglas-Gallardo, O. A.; Sánchez, C. G. Interplay between Intra- and Interband Transitions Associated with the Plasmon-Induced Hot Carrier Generation Process in Silver and Gold Nanoclusters. *J. Phys. Chem. C* **2020**, *124* (2), 1631–1639.
(28) Wu, X.; Liu, B.; Frauenheim, T.; Tretiak, S.; Yam, C.; Zhang, Y. Investigation of Plasmon Relaxation Mechanisms Using Nonadiabatic Molecular Dynamics. *J. Chem. Phys.* **2022**, *157* (21), 214201.
(29) Douglas-Gallardo, O. A.; Berdakin, M.; Frauenheim, T.; Sánchez, C. G. Plasmon-Induced Hot-Carrier Generation Differences in Gold and Silver Nanoclusters. *Nanoscale* **2019**, *11* (17), 8604–8615.
(30) Govorov, A. O.; Zhang, H. Kinetic Density Functional Theory for Plasmonic Nanostructures: Breaking of the Plasmon Peak in the Quantum Regime and Generation of Hot Electrons. *J. Phys. Chem. C* **2015**, *119* (11), 6181–6194.
(31) Brown, A. M.; Sundararaman, R.; Narang, P.; Goddard, W. A.; Atwater, H. A. Nonradiative Plasmon Decay and Hot Carrier Dynamics: Effects of Phonons, Surfaces, and Geometry. *ACS Nano* **2016**, *10* (1), 957–966.
(32) Scholl, J. A.; Koh, A. L.; Dionne, J. A. Quantum Plasmon Resonances of Individual Metallic Nanoparticles. *Nature* **2012**, *483* (7390), 421–427.
(33) Guidez, E. B.; Aikens, C. M. Theoretical Analysis of the Optical Excitation Spectra of Silver and Gold Nanowires. *Nanoscale* **2012**, *4* (14), 4190.
(34) Liu, Z.; Oviedo, M. B.; Wong, B. M.; Aikens, C. M. Plasmon-Induced Excitation Energy Transfer in Silver Nanoparticle Dimers: A Real-Time TDDFTB Investigation. *J. Chem. Phys.* **2022**, *156* (15), 154705.
(35) Niehaus, T. A.; Suhai, S.; Della Sala, F.; Lugli, P.; Elstner, M.; Seifert, G.; Frauenheim, Th. Tight-Binding Approach to Time-Dependent Density-Functional Response Theory. *Phys. Rev. B* **2001**, *63* (8), 085108.
(36) Giri, S. K.; Schatz, G. C. Photodissociation of H_2 on Ag and Au Nanoparticles: Effect of Size and Plasmon versus Interband Transitions on Threshold Intensities for Dissociation. *J. Phys. Chem. C* **2023**, acs.jpcc.3c00006.

(37) Asadi-Aghbolaghi, N.; Rüger, R.; Jamshidi, Z.; Visscher, L. TD-DFT+TB: An Efficient and Fast Approach for Quantum Plasmonic Excitations. *J. Phys. Chem. C* **2020**, *124* (14), 7946–7955.
(38) Jamshidi, Z.; Asadi-Aghbolaghi, N.; Morad, R.; Mahmoudi, E.; Sen, S.; Maaza, M.; Visscher, L. Comparing the Nature of Quantum Plasmonic Excitations for Closely Spaced Silver and Gold Dimers. *J. Chem. Phys.* **2022**, *156* (7), 074102.
(39) Hull, O. A.; Aikens, C. M. Theoretical Investigations on the Plasmon-Mediated Dissociation of Small Molecules in the Presence of Silver Atomic Wires. *J. Phys. Chem. A* **2023**, *127* (10), 2228–2241.
(40) Yan, L.; Ding, Z.; Song, P.; Wang, F.; Meng, S. Plasmon-Induced Dynamics of H_2 Splitting on a Silver Atomic Chain. *Appl. Phys. Lett.* **2015**, *107* (8), 083102.
(41) Wu, Q.; Zhou, L.; Schatz, G. C.; Zhang, Y.; Guo, H. Mechanistic Insights into Photocatalyzed H_2 Dissociation on Au Clusters. *J. Am. Chem. Soc.* **2020**, *142* (30), 13090–13101.
(42) Hull, O. A.; Lingerfelt, D. B.; Li, X.; Aikens, C. M. Electronic Structure and Nonadiabatic Dynamics of Atomic Silver Nanowire–N_2 Systems. *J. Phys. Chem. C* **2020**, *124* (38), 20834–20845.
(43) Herring, C. J.; Montemore, M. M. Mechanistic Insights into Plasmonic Catalysis by Dynamic Calculations: O_2 and N_2 on Au and Ag Nanoparticles. *Chem. Mater.* **2023**, *35* (4), 1586–1593.
(44) Idrobo, J. C.; Walkosz, W.; Yip, S. F.; Öğüt, S.; Wang, J.; Jellinek, J. Static Polarizabilities and Optical Absorption Spectra of Gold Clusters (Au_n , n = 2 – 14 and 20) from First Principles. *Phys. Rev. B* **2007**, *76* (20), 205422.
(45) Wang, J.; Wang, G.; Zhao, J. Density-Functional Study of Aun (N= 2 –20) Clusters: Lowest-Energy Structures and Electronic Properties. *Phys. Rev. B* **2002**, *66* (3), 035418.
(46) Zhou, M.; Jin, R. Optical Properties and Excited-State Dynamics of Atomically Precise Gold Nanoclusters. *Annu. Rev. Phys. Chem.* **2021**, *72* (1), 121–142.
(47) Pandeya, P.; Aikens, C. M. Real-Time Electron Dynamics Study of Plasmon-Mediated Photocatalysis on an Icosahedral Al_{13}^{-1} Nanocluster. *J. Phys. Chem. A* **2021**, *125* (22), 4847–4860.
(48) Li, X.; Tully, J. C.; Schlegel, H. B.; Frisch, M. J. *Ab Initio* Ehrenfest Dynamics. *J. Chem. Phys.* **2005**, *123* (8), 084106.
(49) Ding, F.; Goings, J. J.; Liu, H.; Lingerfelt, D. B.; Li, X. Ab Initio Two-Component Ehrenfest Dynamics. *J. Chem. Phys.* **2015**, *143* (11), 114105.
(50) Kuda-Singappulige, G. U.; Aikens, C. M. Theoretical Insights into Excitation-Induced Oxygen Activation on a Tetrahedral Ag_8 Cluster. *J. Phys. Chem. A* **2021**, *125* (43), 9450–9458.
(51) Yabana, K.; Nakatsukasa, T.; Iwata, J.-I.; Bertsch, G. F. Real-Time, Real-Space Implementation of the Linear Response Time-Dependent Density-Functional Theory. *Phys. Status Solidi B* **2006**, *243* (5), 1121–1138.
(52) Goings, J. J.; Lestrange, P. J.; Li, X. Real-time Time-dependent Electronic Structure Theory. *WIREs Comput. Mol. Sci.* **2018**, *8* (1).
(53) Perdew, J. P.; Burke, K.; Ernzerhof, M. Generalized Gradient Approximation Made Simple. *Phys. Rev. Lett.* **1996**, *77* (18), 3865–3868.
(54) Rohrdanz, M. A.; Martins, K. M.; Herbert, J. M. A Long-Range-Corrected Density Functional That Performs Well for Both Ground-State Properties and Time-Dependent

Density Functional Theory Excitation Energies, Including Charge-Transfer Excited States. *J. Chem. Phys.* **2009**, *130* (5), 054112.
(55) Hay, P. J.; Wadt, W. R. *Ab Initio* Effective Core Potentials for Molecular Calculations. Potentials for K to Au Including the Outermost Core Orbitals. *J. Chem. Phys.* **1985**, *82* (1), 299–310.
(56) Wadt, W. R.; Hay, P. J. *Ab Initio* Effective Core Potentials for Molecular Calculations. Potentials for Main Group Elements Na to Bi. *J. Chem. Phys.* **1985**, *82* (1), 284–298.
(57) Hay, P. J.; Wadt, W. R. *Ab Initio* Effective Core Potentials for Molecular Calculations. Potentials for the Transition Metal Atoms Sc to Hg. *J. Chem. Phys.* **1985**, *82* (1), 270–283.
(58) Gaussian Development Version, Revision I.13+, M. J. Frisch, G. W. Trucks, H. B. Schlegel, G. E. Scuseria, M. A. Robb, J. R. Cheeseman, G. Scalmani, V. Barone, G. A. Petersson, H. Nakatsuji, X. Li, M. Caricato, A. V. Marenich, J. Bloino, B. G. Janesko, R. Gomperts, B. Mennucci, H. P. Hratchian, J. V. Ortiz, A. F. Izmaylov, J. L. Sonnenberg, D. Williams-Young, F. Ding, F. Lipparini, F. Egidi, J. Goings, B. Peng, A. Petrone, T. Henderson, D. Ranasinghe, V. G. Zakrzewski, J. Gao, N. Rega, G. Zheng, W. Liang, M. Hada, M. Ehara, K. Toyota, R. Fukuda, J. Hasegawa, M. Ishida, T. Nakajima, Y. Honda, O. Kitao, H. Nakai, T. Vreven, K. Throssell, J. A. Montgomery, Jr., J. E. Peralta, F. Ogliaro, M. J. Bearpark, J. J. Heyd, E. N. Brothers, K. N. Kudin, V. N. Staroverov, T. A. Keith, R. Kobayashi, J. Normand, K. Raghavachari, A. P. Rendell, J. C. Burant, S. S. Iyengar, J. Tomasi, M. Cossi, J. M. Millam, M. Klene, C. Adamo, R. Cammi, J. W. Ochterski, R. L. Martin, K. Morokuma, O. Farkas, J. B. Foresman, and D. J. Fox, Gaussian, Inc., Wallingford CT, 2018.
(59) Wang, Y.; Aikens, C. M. Effects of Field Strength and Silver Nanowire Size on Plasmon-Enhanced N_2 Dissociation. *J. Phys. Chem. A* **2023**, acs.jpca.3c00120.
(60) Ding, F.; Guidez, E. B.; Aikens, C. M.; Li, X. Quantum Coherent Plasmon in Silver Nanowires: A Real-Time TDDFT Study. *J. Chem. Phys.* **2014**, *140* (24), 244705.
(61) Liang, W.; Isborn, C. M.; Li, X. Laser-Controlled Dissociation of $C_2H_2^{2+}$: Ehrenfest Dynamics Using Time-Dependent Density Functional Theory. *J. Phys. Chem. A* **2009**, *113* (15), 3463–3469.

TOC Graphic